Chemical Engineering Journal 165 (2010) 290–300

Contents lists available at ScienceDirect

Chemical Engineering Journal

journal homepage: www.elsevier.com/locate/cej

Gas–liquid Taylor flow in square micro-channels: New inlet geometries and interfacial area tuning

Arnaud Leclerc, Régis Philippe*, Vivian Houzelot, Daniel Schweich, Claude de Bellefon

Laboratoire de Génie des Procédés Catalytiques (LGPC) UMR 2214 CNRS/CPE Lyon, Université de Lyon, 43 boulevard du 11 Novembre 1918, 69616 Villeurbanne Cedex, France

ARTICLE INFO

Article history:
Received 12 April 2010
Received in revised form 3 August 2010
Accepted 8 August 2010

Keywords:
Micro-channel
T-junction
Gas–liquid Taylor flow
Inlet geometry
Interfacial area

ABSTRACT

Effects of different T-junction injectors on the generation of a N_2–water Taylor flow has been investigated experimentally in a channel of 300 μm by 300 μm. 4 different inlet geometries and 2 feeding configurations are evaluated in a wide range of fluid flow rates ratio $0 < Q_G/Q_L < 35$. It has been demonstrated that for a given flow rate ratio different patterns of the unit cell (1bubble + 1 slug) can be formed showing the impact of inlet geometries. An attempt to rationalize the result is proposed using a Garstecki-type scaling law for bubble length prediction. A unique geometrically based scaling law is discussed and a quite good agreement is obtained to describe the whole set of experiments, provided that there is no bubble coalescence:

$$\frac{L_{\text{bubble}}}{w_G} = 1.03 \cdot \left(\frac{w_G \cdot w_L}{w_{\text{channel}}^2}\right)^{0.33} + 2.17 \cdot \left(\frac{w_G}{w_L}\right) \cdot \frac{U_G}{U_L}$$

Finally an analysis in terms of specific interfacial area location (caps or bubble body) is proposed showing the interest of such inlet geometries to tune this parameter for fixed fluid flow rates and opening new possibilities for local mass transfer studies in the G–L Taylor flow configuration in square micro-channels.

1. Introduction

Controlling the interfacial area and enhancing the mass transfer in reactive multiphase flows is of great importance in chemical engineering. The use of micro-channels in the Taylor flow regime is one of the possible ways to achieve this goal for G–L mass transfer-limited reactive systems through a careful control of the G–L interface and flow pattern at a local scale [1–3].

The gas–liquid Taylor flow regime consists of an alternating sequence of gas bubbles and liquid slugs. The diameter of the gas bubbles is in the range of the hydraulic diameter of the channel and their length is larger than the hydraulic diameter. If the channel wall exhibits a good wettability by the liquid, it is covered by a thin liquid layer and the gas bubbles are sliding over this “lubricating” film. For the specific case of non-circular channels, there is also liquid, confined along the corners, that connects two adjacent liquid segments. The main key advantages of the Taylor flows are:

(a) Channel-induced geometrical constraint at small scale on the gas–liquid flow that results in laminar regime, high surface area, secondary effect of gravitational force, coalescence and breakage control.
(b) Existence of back-mixing loops inside liquid slugs that ensure an efficient renewal of the liquid layer near the G–L interface and so an enhanced mass transfer by a convective phenomenon [3–5].
(c) The moving of almost isolated gas and liquid compartments for small capillary numbers (<0.01) resulting in a very low axial dispersion [1,2].

In the field of continuous reactors, depending on the reaction constraints (stoichiometry, residence time, targeted productivity, limited pressure drop, etc.), the ranges of liquid and gas flow rates are often correlated and restricted. As a consequence, in a process intensification framework, it appears very interesting to be able to tune hydrodynamic characteristics such as the bubble and slug lengths for a given set of fluid flow rates and channel geometry.

Characterization and modelling of the formation of Taylor flows has been widely investigated in the past years [6–12]. Many authors studied the effects of volumetric flow rates and fluid physical properties on the hydrodynamic behaviour observed. When a scaling law is proposed, two main approaches are observed. The first one consists in comparing the characteristic times and lengths of the main physical processes (capillarity, viscosity, inertia, gravity, etc.)

---

* Corresponding author. Tel.: +33 (0)4 72 43 17 59; fax: +33 (0)4 72 43 16 73.
E-mail address: regis.philippe@lgpc.cpe.fr (R. Philippe).

1385-8947/$ – see front matter © 2010 Elsevier B.V. All rights reserved.
doi:10.1016/j.cej.2010.08.021

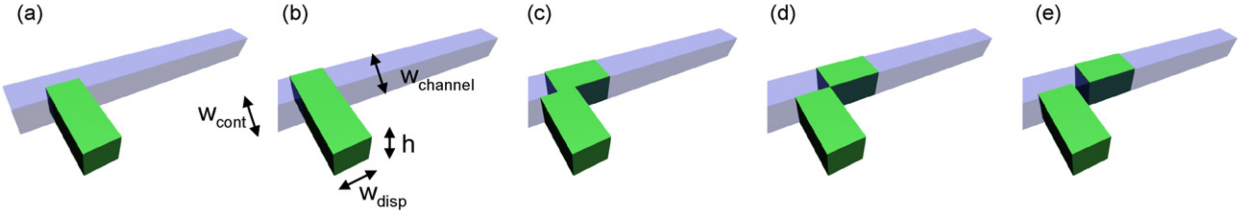

Fig. 1. Illustrations of the geometrical model of Garstecki et al.

involved through dimensionless numbers (Ca, We, Bo, Re,. . .). This analysis uses only the physical and flow characteristics of the fluids without taking into account precise geometrical details. The other approach is mainly based on geometrical considerations and mass conservation as illustrated by Fig. 1. This second way arises from the work of Garstecki et al. [12].

1.1. The Garstecki model for bubble formation and its derivations

In their pioneering work, Garstecki et al. [12] derived a quasi-static model (Ca and We $\ll 1$) for the prediction of segment length of water dispersed in an oil flow using a T-shaped injector and a square micro-channel.

This description is only based on geometrical considerations and describes with box-like objects the dispersed phase segment formation (Fig. 1). This elegant model contains three steps:

- Step 1: The dispersed phase enters the main channel until occupying the whole accessible volume V_1 during a time t_1 (Fig. 1a and b and Eq. (1)):

$$V_1 = w_{\text{disp}} \cdot h \cdot w_{\text{cont}} \quad \text{and} \quad t_1 = \frac{V_1}{Q_{\text{disp}}} \tag{1}$$

- Step 2: This cubic segment is then (and only then) progressively pinched by the flowing continuous phase. During this step, the moving segment is still fed with dispersed phase allowing a volume V_2 to be added during a time t_2 (Fig. 1c and d and Eq. (2)):

$$V_2 = \frac{V_1}{Q_{\text{cont}}} \cdot Q_{\text{disp}} \quad \text{and} \quad t_2 = \frac{V_1}{Q_{\text{cont}}} \tag{2}$$

- Step 3: Finally, the dispersed phase segment is squeezed at a total volume $V = V_1 + V_2$ (Fig. 1e), corresponding to a reduced length $L_{\text{disp}}/w_{\text{disp}}$ given by Eq. (3).

$$\frac{L_{\text{disp}}}{w_{\text{disp}}} = 1 + \frac{Q_{\text{disp}}}{Q_{\text{cont}}} \tag{3}$$

In order to take into account the real form of the segments and the flowing continuous phase into the corners (see Fig. 2), the authors proposed to use additional parameters α and β which are inserted and adjusted to give the famous scaling law of Garstecki et al. given in Eq. (4).

$$\frac{L_{\text{disp}}}{w_{\text{disp}}} = \beta + \alpha \cdot \frac{Q_{\text{disp}}}{Q_{\text{cont}}} \tag{4}$$

Finally, relations can be derived using the ratio of the phase velocities at the inlet instead of the flow rates ratio (Eq. (5)) in order to take into account different gas inlet widths [13]:

$$\frac{L_{\text{disp}}}{w_{\text{disp}}} = \beta + \alpha' \cdot \frac{U_{\text{disp}}}{U_{\text{cont}}} \tag{5}$$

Many authors used Eq. (4) and fitted α and β for various channel geometries and fluid properties. Although most values are of the order of unity, the scattering is not clearly explained. A potential explanation can be found in the geometrical properties of the connecting device where the fluids meet each other.

1.2. Recent work on inlet geometry considerations for G–L Taylor flows

It's only very recently that researchers take into account inlet geometry. Fries et al. [14] and Tan et al. [15] studied experimentally the impact of the angle between gas and liquid flows for an "italic T"-junction. Both found scaling laws for bubble length dependant of the slant angle. The impact of the width of the lateral gas inlet channel has also been investigated either experimentally [14] or numerically [13]. T-junctions are not the only ones studied: for example, Dietrich et al. [16] studied the effect of intersection angle in the case of a flow focusing X-device and Shao et al. [17] performed simulations on the effect of the gas nozzle diameter inside a co-axial injector. Table 1 summarizes the different scaling laws obtained and their domain of validity. Later on, given that gas–liquid flow will only be considered, the subscripts "cont" relative to the continuous wetting phase will be replaced by "L" or "slug". Similarly, the subscript "disp" relative to the dispersed phase will be replaced by "G" or "bubble".

The last column of Table 1 gives an example of bubble length predicted with these correlations in the case of a nitrogen and water flow with identical fluid flow rates. It allows to show the variability of these scaling laws.

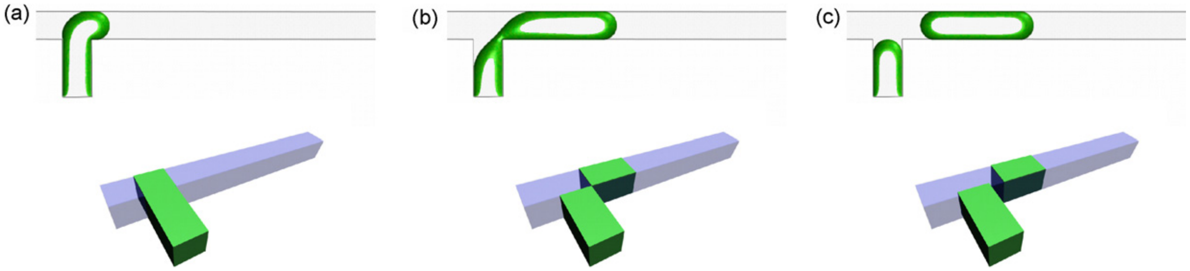

Fig. 2. Comparison of sketches of dispersed phase segments obtained by CFD and by the "box-like" Garstecki model: (a) during the first step, (b) during the second step and (c) after total formation.

Table 1
Scaling laws for bubble and slug generation of the literature.

Injector and Ref.	Parameter	Scaling law	Example L_b (μm)
T-junction [13]	W_G	$\frac{L_{bubble}}{w_{channel}} = 3 + 0.8 \frac{Q_G}{Q_L} \frac{A_G}{A_{channel}}$	1380
T-junction [14]	Angle θ and w_G	$\frac{L_{bubble}}{w_{channel}} = 1 + \alpha \frac{Q_G}{Q_L}$ with $\alpha = \frac{17.21}{(w_G/w_{channel})\theta^{1/2}}$ $\frac{L_{slug}}{w_{channel}} = 2.9 \left[\left(\frac{Re}{Ca} \right)^{1/3} \frac{\varepsilon_L^*}{(w_G/w_{channel})^{2.5}\theta} \right] + 3.15$	1393
T-junction [15]	Angle θ	$\frac{L_{bubble}}{w_G} = \frac{1}{2} \left(\frac{Q_G}{Q_L} \sin\theta + \frac{2}{5} \text{cotan}\,\theta \right)^{1/2} \text{Ca}^{-1/5}$	393
X-junction (flow focusing) [16]	Angle θ	$\frac{L_{bubble}}{w_G} = \beta \left(\frac{Q_G}{Q_L} \right)^{\alpha}$ with $\alpha = \frac{1}{4} \frac{w_G}{w_{channel}} + \frac{1}{9}$ and $\beta = 8.3 \left(\frac{\theta}{\theta_{ref}} \right)^{-1/8} \left(\frac{\sigma}{\sigma_{ref}} \right) \left(\frac{\mu}{\mu_{ref}} \right)^{1/10}$	2961
Co-axial [17]	$w_{nozzle,G}$	No scaling law	–

Example: $\theta = 90^\circ$, $h = w_{channel} = w_G = w_L = 300$ μm, $Q_G = 200$ μL/min, $Q_L = 100$ μL/min.

1.3. Objective of this study

The aim of the present work is to study the effect of four new different T-junction geometries on the Taylor flow formation and for each one, two configurations of fluid feed. A large range of liquid and gas flow rates was studied; an attempt to rationalize the description of the bubble formation based on a Garstecki approach is proposed and finally an analysis of the generated surface area and its location (caps or body of the bubbles) is proposed.

2. Experimental

The microfluidic chips used in this work were manufactured at the CEA LETI (Grenoble, France) from a silicon wafer and a glass wafer sealed by anodic bonding. Channels were etched on silicon by Deep Reactive Ion Etching (DRIE). The main channel presents a constant square section of 300 μm by 300 μm. Fig. 3a and b presents respectively an overview of the two chips and a zoom on the 4 T-junctions used in this study. In any cases, the depth of the channel is constant and equal to 300 μm.

For each T injector, two feeding configurations are tested. The "straight feed" (Fig. 4a) consists in feeding the dispersed gas phase in the lateral channel perpendicular to the main channel. The "right angle feed" (Fig. 4b) consists in feeding the wetting liquid phase in the lateral channel. In general, "right angle" and "straight" refers to the wetting fluid.

The experimental set up is schematized in Fig. 5. It consists of a massflow controller Bronkhorst "el flow" for the nitrogen feed (able to deliver up to 1 mL/min NTP) and a syringe pump PHD 4400 of Harvard Apparatus for the deionised water feed. Depending on the liquid flow, pressure varies in the range 1–5 bar. The connection to the Si-chip is ensured by silica capillaries (100 μm i.d., 250 μm o.d.) glued with Epoxy glue Ecobond 144 A from Emerson & Cuming. The chip is fixed on a copper support maintained at 20 °C. The exact temperature is recorded with a thermocouple. A stereo-binocular magnifier Zeiss discovery V20, a fast camera Optronis CR600 × 2 and an acquisition interface Coreco PC2Vision connected to a computer were used to record sequences at a rate up to 10,000 frames per second. Measurements in this study are mainly made at a rate of 1000 frames per second.

Table 2 summarizes the experimental details of our experiments. For each injector and each feeding configuration, three inlet flow rates of Gas are employed: 200, 300 and 400 NμL/min. For each gas flow rate, 8 liquid flow rates are tested: 10, 20, 40, 60, 80,

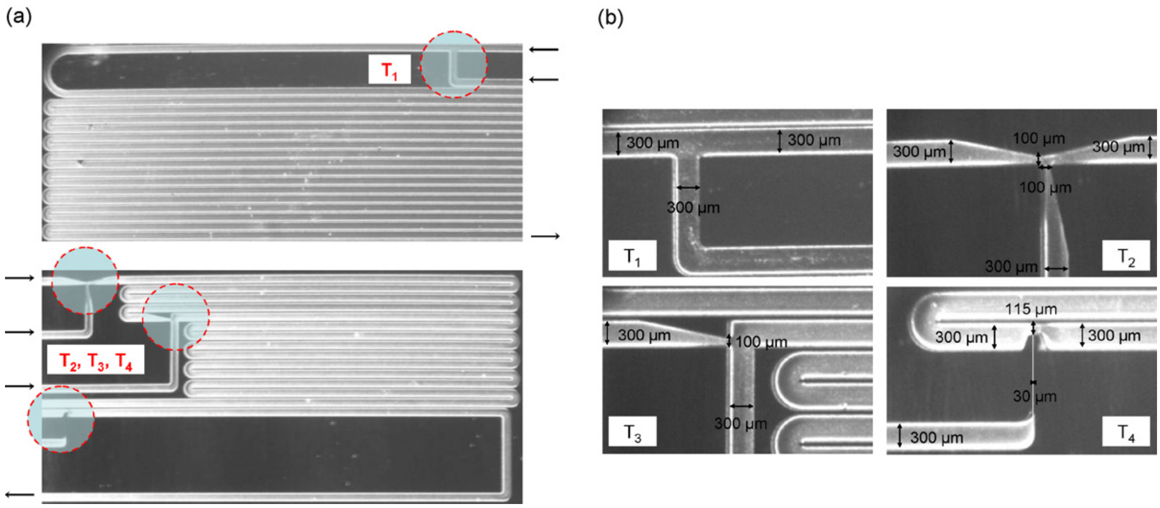

Fig. 3. (a) Silicon chips used in this study and (b) Zoom in the inlet regions with theirs dimensions.

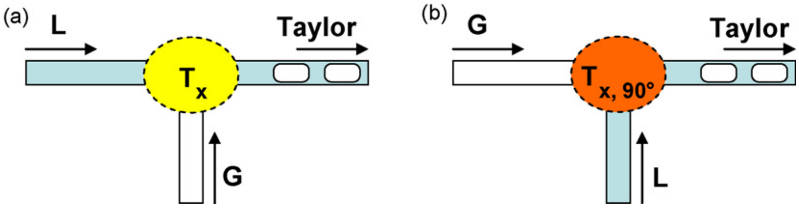

Fig. 4. Feeding configurations studied: (a) "straight" and (b) "right angle" configurations.

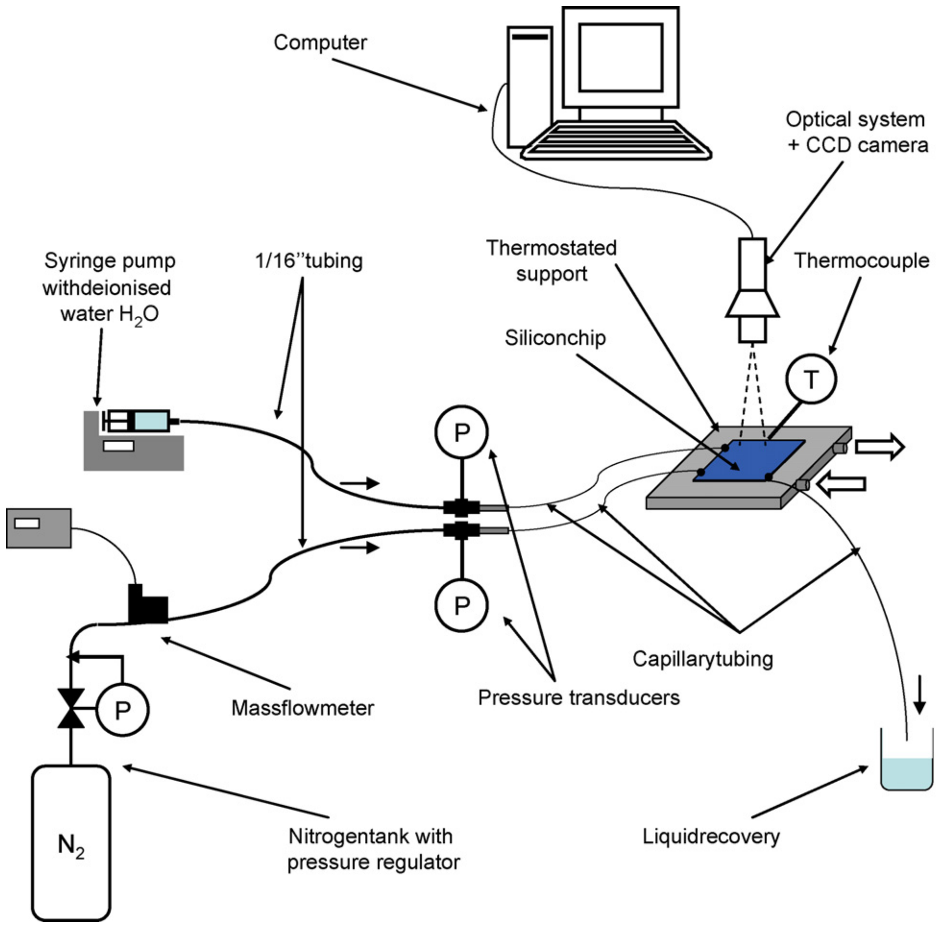

Fig. 5. Experimental setup overview.

100, 150 and 200 μL/min. Corresponding gas and liquid Reynolds numbers are very low: $0.8 < Re_G < 5.1$ and $8.2 < Re_L < 25.1$ (based on the mean fluid velocity and the size of the main channel). Our experimental schedule consists in $4 \times 2 \times 3 \times 8 = 192$ experiments.

After stabilization of the pressure, a sequence of 3 s is recorded at a rate of 1000 frames per second. Careful measurements of 10 slug lengths and 10 bubble lengths are made on different pictures of this sequence in the main channel between the T-junction and the first U-turn (see Fig. 3a). This method is systematically applied to each experiment allowing to obtain a meaningful value of bubble and slug lengths for further calculations. Measurements are made along the axis of the channel from the rear to the front ends of bubbles and slugs. Repeated measurements lead to standard deviations in the range of 1–2% for the majority of slugs and bubbles. Deviations near 8% can be reached for the smallest objects (in the range of 100 μm).

3. Taylor flow geometrical description

For square capillaries, depending on the balance between surface forces and viscous forces (through the Ca number), there are two main bubble configurations: axisymetrical for Ca > 0.1 and non-axisymetrical for Ca < 0.1 [18] (see Fig. 6).

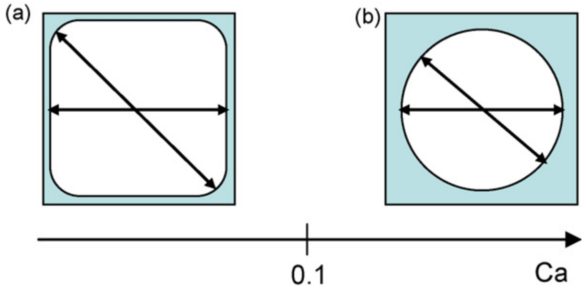

Fig. 6. Shapes of gas bubbles in square micro-channel: (a) non-axisymetrical and (b) axisymetrical.

Given that this work is made in a range of very low Ca numbers ($10^{-4} < Ca < 10^{-3}$, based on the mean velocity in the main channel) it appears obvious to choose a non-axisymetrical bubble geometrical approach. A schematic of different descriptors of our geometrical model is given in Fig. 7.

A bubble is assumed to be made of 2 ideal hemispherical caps and of a cylindrical body of square cross section with rounded corners. Far away from these corners, there is a liquid film of thickness δ, which is estimated by the correlation of Hazel and Heil [19]. This

Table 2
Experimental details.

Injectors	Feeding configuration	T (°C)	P (bar)	Gas inlet flow rate (NμL/min)	Liquid inlet flow rate (μL/min)
T_1–T_4	"Straight" and "right angle"	20	Varying from 1 to 5 (related to the flow rates)	200, 300 and 400	10, 20, 40, 60, 80, 100, 150 and 200

Table 3
Expressions derived in our geometrical description of Taylor flow.

Object	Expressions
Unit cell	$V_{\text{unitcell}} = (L_{\text{b}} + L_{\text{s}})w^2_{\text{channel}}$ (volume)
Film	$\delta = 0.003 \cdot w_{\text{channel}}$ (for Ca < 0.04) [18] (thickness)
Bubble	$S^{\text{ext}}_{\text{bubble}} = S^{\text{ext}}_{\text{2caps}} + S^{\text{ext}}_{\text{body}}$ (external surface) $V_{\text{bubble}} = V_{\text{2caps}} + V_{\text{body}}$ (volume)
Bubble caps	$S^{\text{ext}}_{\text{2caps}} = \pi(w_{\text{channel}} - 2\delta)^2$ (external surface) $V_{\text{2caps}} = \frac{\pi}{6}(w_{\text{channel}} - 2\delta)^3$ (volume)
Bubble body	$L_{\text{body}} = L_{\text{bubble}} - w_{\text{channel}} + 2\delta$ (length) $r_{\text{corner}} = \frac{w_{\text{channel}} - 2\delta}{4}$ (radius of the 4 round corners of the cross section) $P_{\text{body}} = \left(\frac{\pi}{2} + 2\right)(w_{\text{channel}} - 2\delta)$ (perimeter of the cross section) $S^{\text{ext}}_{\text{body}} = P_{\text{body}} L_{\text{body}}$ (external surface) $S_{\text{body}} = (1 - W)w^2_{\text{channel}}$ (cross section) $W = \frac{4\delta}{w_{\text{channel}}}\left(1 - \frac{\delta}{w_{\text{channel}}}\right) + \frac{4-\pi}{w^2_{\text{channel}}}\left(\frac{w_{\text{channel}}}{4} - \frac{\delta}{2}\right)^2$ (fraction of the cross section of a channel remaining for the gutters and the film) $V_{\text{body}} = (1 - W)w^2_{\text{channel}} L_{\text{body}}$ (volume)
Gutters	$V_{\text{gutters}} = W w^2_{\text{channel}} L_{\text{body}}$ (volume)
Slug	$V_{\text{slug}} = V_{\text{unitcell}} - V_{\text{bubble}} - V_{\text{gutters}}$ (volume) $V_{\text{slug}} = (L_{\text{slug}} + w_{\text{channel}} - 2\delta)w^2_{\text{channel}} - \frac{\pi}{6}(w_{\text{channel}} - 2\delta)^3$ (volume)
Caps specific surface area	$a_{\text{2caps}} = \frac{S^{\text{ext}}_{\text{2caps}}}{V_{\text{unitcell}}} = \frac{\pi(w_{\text{channel}} - 2\delta)^2}{w^2_{\text{channel}}(L_{\text{bubble}} + L_{\text{slug}})}$
Body specific surface area	$a_{\text{body}} = \frac{S^{\text{ext}}_{\text{body}}}{V_{\text{unitcell}}} = \frac{((\pi/2)+2)(w_{\text{channel}} - 2\delta)(L_{\text{bubble}} - w_{\text{channel}} + 2\delta)}{w^2_{\text{channel}}(L_{\text{bubble}} + L_{\text{slug}})}$
Total specific surface area	$a = a_{\text{body}} + a_{\text{2caps}} = \frac{(w_{\text{channel}} - 2\delta)[(2+(\pi/2))L_{\text{bubble}} - ((\pi/2)+2)w_{\text{channel}} + (4-\pi)\delta]}{w^2_{\text{channel}}(L_{\text{bubble}} + L_{\text{slug}})}$
Gas phase retention	$\varepsilon_{\text{G}} = \frac{V_{\text{bubble}}}{V_{\text{unitcell}}} = \frac{\frac{\pi}{6}(w_{\text{channel}} - 2\delta)^3 + (1-W)w^2_{\text{channel}}(L_{\text{bubble}} - w_{\text{channel}} + 2\delta)}{(L_{\text{bubble}} + L_{\text{slug}})w^2_{\text{channel}}}$

description is approximate since the transition from the osculating hemisphere of the real cap to the “rounded-square” cylinder is ignored. Table 3 presents expressions for lengths, surfaces, cross sections and volumes that are involved in this model, and that can be obtained directly from a careful measurement of the bubble and slug lengths as shown in Fig. 7. Details of the calculations are given in the supporting information SI 1.

4. Results and discussion

4.1. Bubble and slug lengths

Fig. 8 shows the Taylor flows obtained with our 4 injectors for 3 different ratios of gas to liquid flow rates. Frames of the 192 experiments are also given in the supplementary informations (SI 2–5) of this article. Cases (a)–(c) almost spans the whole range of stable Taylor flow. Within each case the flow rate ratio is almost the same, and it is easily seen that the bubble size and their number depend significantly on the type of junction and on flow configuration.

It is an important result that comes in contrast with the different descriptions of bubble formation that use power laws of dimensionless numbers which neglect inlet geometry variations. The second important result is that T_1 and T_2 injectors which present the same shape of the channels just upstream of the junction (see Fig. 3b), give the same bubbles when the inlet configuration is switched from “straight” to “right angle”. Contrarily, T_3 and T_4 show significant changes. This result gives a novel insight in the influence of the feeding configuration and confirms that superficial velocities and local geometry (dead zones, progressive shrinkage,. . .) at the junction are very important parameters.

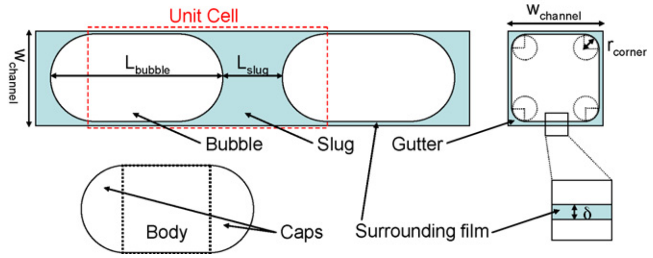

Fig. 7. Unit cell geometrical description.

Figs. 9 and 10 show respectively the evolution of the bubble length L_{bubble} and the slug length L_{slug} against Q_G/Q_L for the injectors in the 2 feed configurations. The measurement was made when the downstream channel reaches a constant cross section (T_2) and when possible bubble coalescence is over.

Injectors T_1 and $T_{1,\,90^\circ}$ behave classically and the observed bubble length evolution is in good agreement with a Garstecki-type law. Feed interchange has no effect on the obtained Taylor flow. This result is not obvious because the squeezing process is geometrically different and thus different behaviours could have been expected.

Injectors T_2 and $T_{2,\,90^\circ}$ which present an identical thinning of the two inlets behave identically. The trends observed with these “symmetrical” injectors are quite similar to those of T_1 and $T_{1,\,90^\circ}$ but with significantly smaller bubbles and slugs. Moreover, near a ratio Q_G/Q_L of 5.0, a sudden increase can be observed in the evolutions of bubble whereas slug length stabilizes. As it is shown in Fig. 11a, a rapid decrease of slug length is observed when Q_G/Q_L increases up to $Q_G/Q_L \approx 5.0$. At this point, after the enlargement of the channel about 1 mm downstream of the junction zone, two successive bubbles become adjacent and coalesce together leading to a redistribution of the liquid into the adjacent slugs through the channel corners. These slugs become longer and thus stable and able to separate two bubbles. After this increase in the slug size due to coalescence near $Q_G/Q_L = 5.0$, slugs seem to stabilize near a value of 100 μm for the higher ratios.

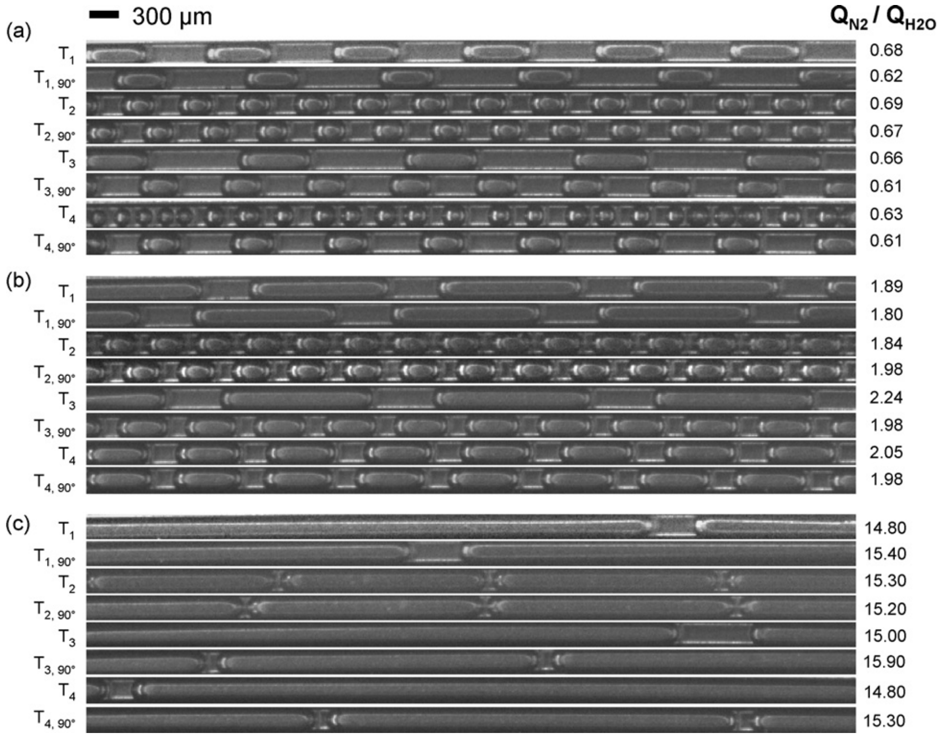

Fig. 8. Obtained Taylor flows for (a) a low ratio (below 1), (b) an intermediate ratio (around 2) and (c) a high ratio of inlet flow rates (around 15).

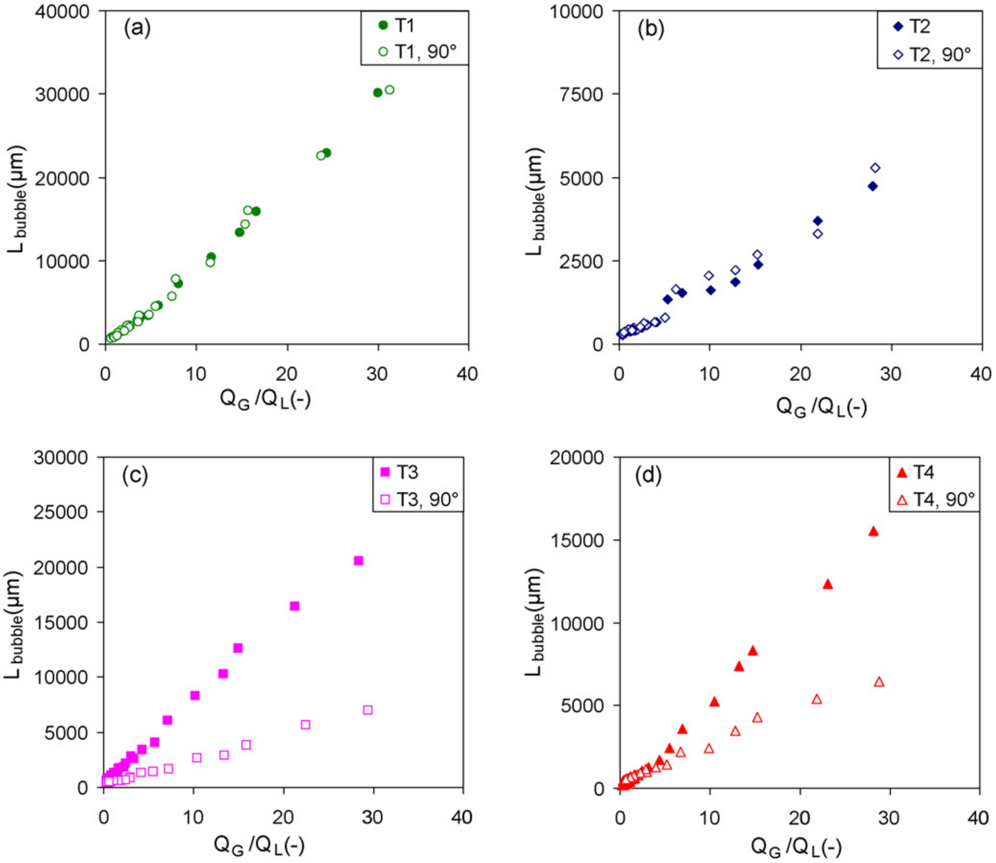

Fig. 9. Evolution of the bubble length against the ratio of fluid flows for (a) T_1 and $T_{1,90^\circ}$, (b) T_2 and $T_{2,90^\circ}$, (c) T_3 and $T_{3,90^\circ}$ and (d) T_4 and $T_{4,90^\circ}$.

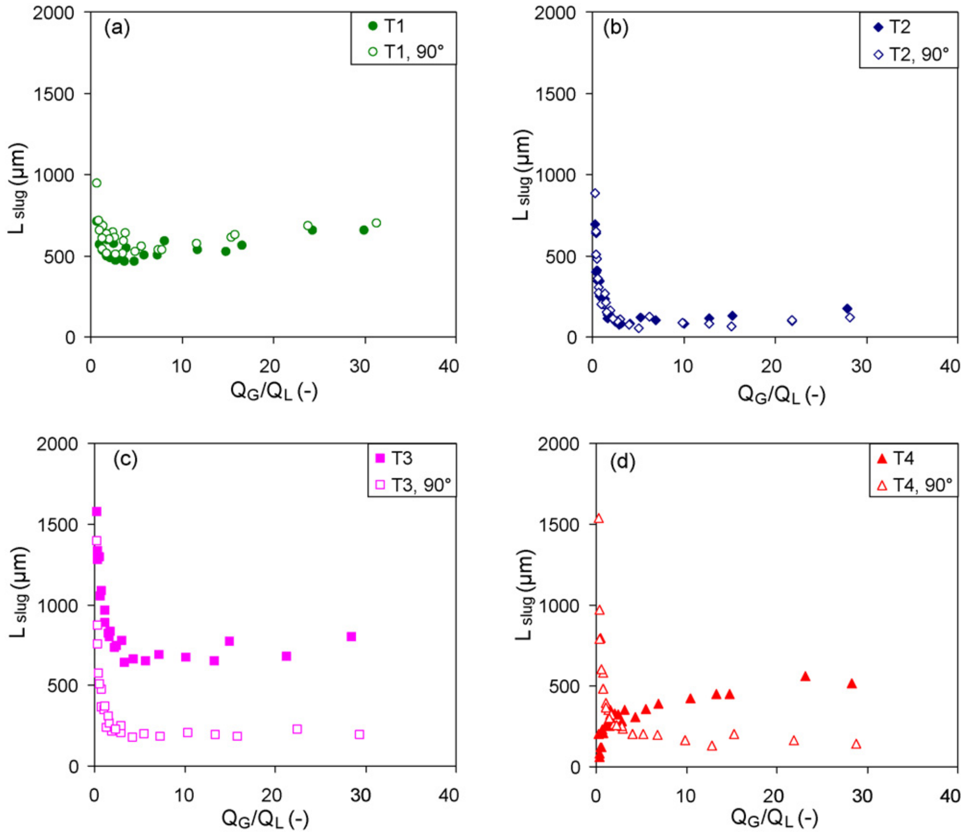

Fig. 10. Evolution of the slug length against the ratio of fluid flows for (a) T_1 and $T_{1,\,90^\circ}$, (b) T_2 and $T_{2,\,90^\circ}$, (c) T_3 and $T_{3,\,90^\circ}$ and (d) T_4 and $T_{4,\,90^\circ}$.

Injectors T_3 and $T_{3,\,90^\circ}$ present a unique (upstream) thinning: for T_3, the liquid inlet is concerned and for $T_{3,\,90^\circ}$ it is the gas inlet. Both are responsible for smaller bubbles and slugs than the classical injector T_1 but the effect of the thinning is more important when located at the gas inlet ($T_{3,\,90^\circ}$). Evolutions of slug lengths are roughly similar to those encountered with T_1 (rapid decrease and stabilization) but the stabilization occurs for different values: approximately 680 µm (quite similar to T_1) for T_3 and 200 µm for $T_{3,\,90^\circ}$. In the range of Q_G/Q_L tested, no coalescence was observed.

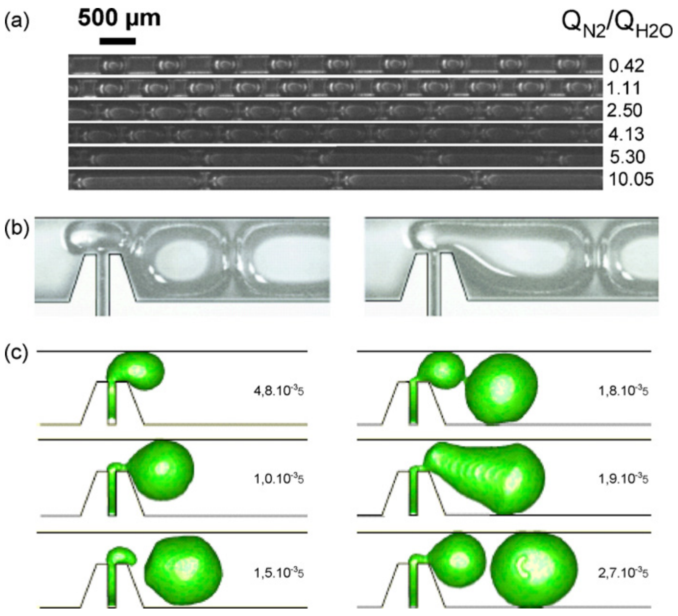

Fig. 11. (a) Evolution of Taylor flow against Q_G/Q_L for T_2 and $T_{2,\,90^\circ}$ showing a transition with coalescence near $Q_G/Q_L = 5$, (b) very fast coalescence in T_4 observed experimentally and (c) numerically (VOF-based simulation).

With injectors T_4 and $T_{4,\,90^\circ}$ presenting two non-identical constrictions (115 µm and 30 µm) we could expect to generate objects smaller than those obtained with T_2 and T_3. $T_{4,\,90^\circ}$ leads effectively to smaller bubbles but T_4 leads to longer objects than T_2. The observed evolution of slug length with T_4 is singular when compared to the other injectors. When the gas is injected by the lateral nozzle (T_4), the slug length increases quickly with Q_G/Q_L and then stabilizes to a value near 550 µm for the higher flow rates ratios. When the liquid is fed through the lateral nozzle ($T_{4,\,90^\circ}$) the slug length behaves identically to the others injectors with a decrease and then a stabilization near 150 µm. The peculiar evolution for T_4 slug and bubble lengths can be explained by a phenomenon of rapid coalescence of small objects at the injector. This has been evidenced by experimental observations (Fig. 11b) and by numerical simulations using a VOF method (not detailed here, see Ref. [20] for supplementary information) using Fluent® software (Fig. 11c). We can see that, as it was expected, shorter and smaller objects are generated by this injector but they coalesce just after their formation near the injector leading to more conventional Taylor bubbles and slugs.

Consequently, according to the exact design of a globally T-shaped gas–liquid junction, it is possible to generate different unit cells of Taylor flow for a given ratio of flow rates in a large range of operations (for $0.25 < Q_G/Q_L < 30$). Thus different hydrodynamic patterns can be obtained (different pressure drops, different recirculation,. . .) and possibly different mass transfer behaviours (k_L). These effects are investigated in a current work and will be presented later. In Section 4.3 of this article, the effect of our injectors on the specific surface area "*a*" will only be discussed.

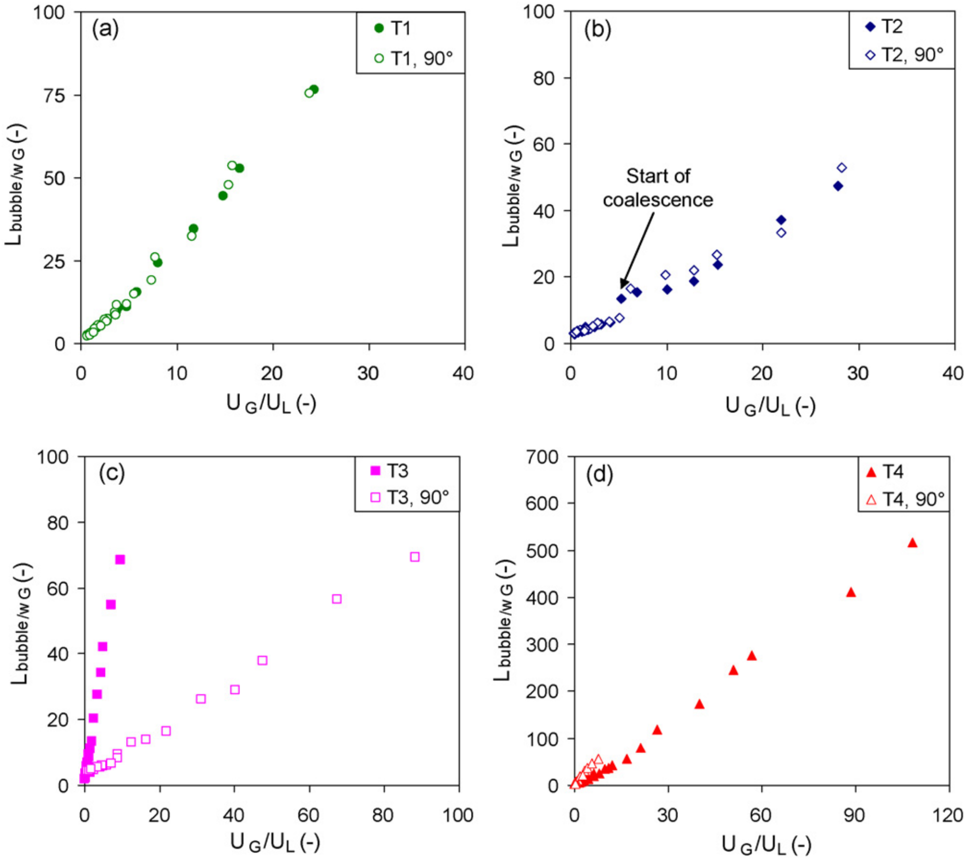

Fig. 12. Garstecki approach for the evolution of bubble length for (a) T_1 and $T_{1,90^\circ}$, (b) T_2 and $T_{2,90^\circ}$, (c) T_3 and $T_{3,90^\circ}$ and (d) T_4 and $T_{4,90^\circ}$.

4.2. Flow formation description

Rationalization of the observed flows for each injector in its two configurations by an approach with a Garstecki-type law has been conducted and is shown in Fig. 12. The dimensionless bubble length (bubble length divided by the width of the gas inlet) is plotted against the fluid inlet velocities ratio U_G/U_L. It appears in Fig. 12 that the bubbles generated in the different injectors (except T_2 and $T_{2,90^\circ}$) for the tested conditions can be described by different Garstecki-type scaling laws. A similar approach is applicable to T_2 and $T_{2,90^\circ}$ by distinguishing the zones before and after coalescence (limit around $U_G/U_L = 5$). Garstecki approach (Eq. (5)) was used to correlate bubble length to flow rate ratio. Table 4 summarizes the obtained α' and β coefficients. Globally and unsurprisingly, it can be seen that quite different coefficients are obtained for our 4 selected geometries. For T_2 and $T_{2,90^\circ}$, the effect of coalescence is only visible in the β coefficient. The value obtained when coalescence is observed is around twice the value obtained without coalescence. This is coherent with the fact that two bubbles coalesce for $U_G/U_L > 5$.

Table 4
"Garstecki-type" scaling laws.

Injector	α'	β	R^2
T_1	2.23	1.25	0.97
$T_{1,90^\circ}$	2.24	1.22	0.96
T_2 (before coalescence)	0.96	2.65	0.98
T_2 (after coalescence)	1.51	4.93	0.96
$T_{2,90^\circ}$ (before coalescence)	0.99	2.92	0.96
$T_{2,90^\circ}$ (after coalescence)	1.52	5.03	0.94
T_3	6.62	1.50	0.98
$T_{3,90^\circ}$	0.74	3.20	0.96
T_4	3.29	3.35	0.98
$T_{4,90^\circ}$	6.86	5.52	0.97

Garstecki approach: $\frac{L_{bubble}}{w_G} = \beta + \alpha' \cdot \frac{U_G}{U_L}$.

Based on these results and on simple geometrical considerations, an attempt to rationalize all the observed flows generated by these different geometries has been made. All the experiments have been taken into account except those where coalescence has been detected: T_2 and $T_{2,90^\circ}$ for $Q_G/Q_L > 5$ and all the experiments carried out with T_4 (straight). Different approaches were tested and the best fitting has been obtained with the following kind of equation:

$$\frac{L_{\text{bubble}}}{w_G} = \beta'' \cdot \left(\frac{w_G \cdot w_L}{w_{\text{channel}}^2}\right)^b + \alpha'' \cdot \left(\frac{w_G}{w_L}\right)^a \cdot \frac{U_G}{U_L} \qquad (6)$$

A classical optimisation based on the minimisation of an objective function S (Eq. (7)) by varying the 4 parameters α'', a, β'' and b has been conducted.

$$S = \sum_N \left(\frac{\left|(L_{\text{bubble}}/w_G)_{\text{exp}} - (L_{\text{bubble}}/w_G)_{\text{calc}}\right|}{(L_{\text{bubble}}/w_G)_{\text{exp}}}\right) \qquad (7)$$

This optimisation leads to the following set of parameters and to the parity plot given in Fig. 13: $\alpha'' = 2.17$; $\beta'' = 1.03$; $a = 1.00$; $b = 0.33$.

The fact that $a = 1.00$ is quite logical and allows to find again the flow rates ratio at the inlet in the scaling law. The term elevated at a power $b = 0.33$ and the power b itself are more complex to explain with a physical sense. However this scaling law leads to a quite good agreement in the prediction of dimensionless bubble lengths for the experiments without coalescence in the case of our different complex geometries.

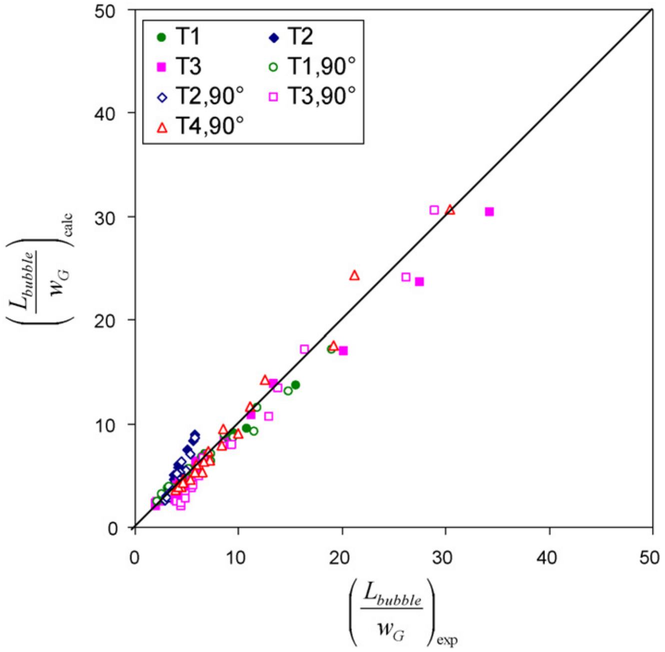

Fig. 13. Parity plot for the dimensionless bubble length prediction with a unique scaling law for all the experiments without coalescence.

4.3. Effect on specific surface area

Since the chemical engineering community started studying the local mass transfer in G–L segmented flow configuration either experimentally [2] or numerically [3], different theories have been discussed on the localisation of the effective surface for mass transfer: Does species mainly transfer at the bubble caps or at the total bubble area? An explanation involving a link between the less or more rapid saturation of the film surrounding the bubble body and the bubble length is given by Kreutzer et al. [1]. This scenario leads effectively to the two following situations:

- Bubble caps surfaces are only effective for mass transfer, the film being quickly saturated.
- Total bubble surfaces are effective for mass transfer with a partially and progressively saturated film.

Thus, given that bubble length and unit cell can be tuned for a given ratio of fluid flow rates by using the different injector designs, significant differences on effective surface area "a" can be expected independently of any impact of hydrodynamics on the mass transfer coefficient "k_L".

Fig. 14 presents the evolution of the total specific surface area "a_{tot}" encountered for the 8 inlet configurations in the framework of our geometrical model (see Table 3). We choose to express the specific surface areas in terms of surface area per unit volume of reactor. In other words, the unit cell volume was chosen as the reference volume.

It can be seen that for a given ratio of fluid flow rates there is almost no impact of the injector geometry and feeding configuration on the generated surface area in the whole range of our experimental domain. This is easily explained geometrically because if $\delta \ll w_{channel} \ll L_{channel}$ and if the no-slip hypothesis are verified, then the expression for a_{tot} in Table 3 reduces to:

$$a_{tot} \approx \frac{2+(\pi/2)}{w_{channel}} \cdot \frac{L_{bubble}}{L_{bubble}+L_{slug}} \approx \frac{2+(\pi/2)}{w_{channel}} \cdot \frac{(Q_G/Q_L)}{1+(Q_G/Q_L)} \quad (\text{in } m^2/m^3) \tag{8}$$

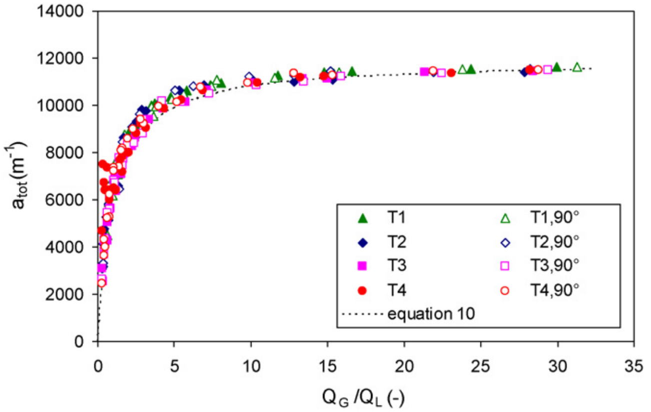

Fig. 14. Evolution of the total specific surface area (a_{tot}) generated for all the injectors with fluid flow rates ratio.

Thus, the specific surface area appears to be only dependant on the fluid flow rates ratio (for the low value of Q_G/Q_L) and of the channel width with an asymptotic value being of 11,900 m^2/m^3. Since the inequality among d, w and L_b holds, the good fit observed in Fig. 14 support to the validity of the no-slip hypothesis. Since the total specific surface area is almost independent of the junction design, it appears more interesting to look at the respective contributions of the bubble caps (a_{caps}) and of the bubble body (a_{body}). Fig. 15 represents the evolution of these two specific surface areas against the fluid flow rates ratio.

Depending on the injector geometry and on the feed configuration, for a same fluid flow rate ratio, a different specific surface area contributions can be obtained, especially for the low ratios ($Q_G/Q_L < 5$), i.e., relatively short bubbles. It can be seen on Fig. 15a

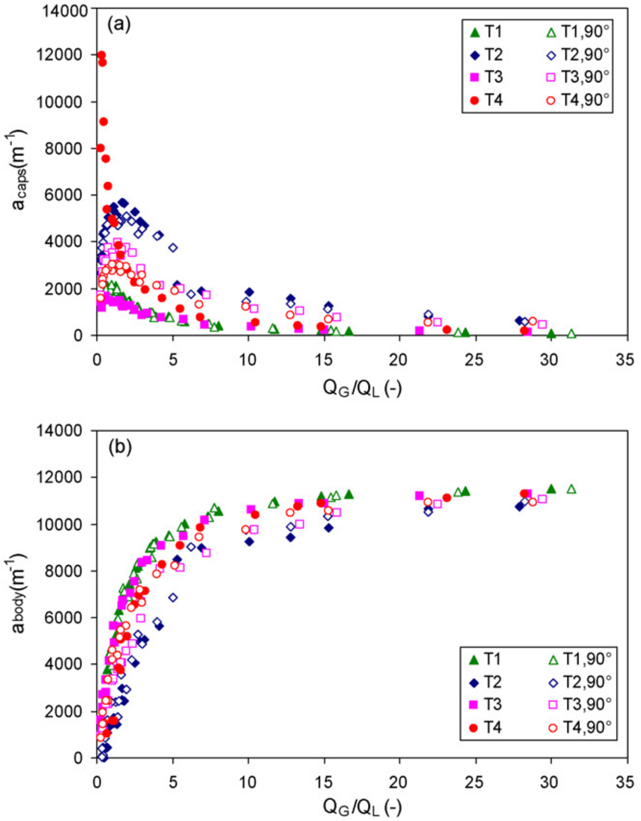

Fig. 15. Effect of inlet geometry and feeding configuration on the evolution of (a) a_{caps} and (b) a_{body} with fluid flow rates ratio.

that for T_4, very high a_{caps} near the asymptotic value of 11,900 m^{-1} are reached due to the spherical bubbles obtained (as it can be seen in SI 5) whereas for injectors T_3 or T_1 a value around 6 times lower is obtained for the same fluid flow rates ratio. This important difference is explained by the fact that with T_4 the limit between Taylor flow and bubbly flow is reached with spherical objects (and so without a bubble cylindrical body) having a diameter near the channel diameter whereas for the same ratio of fluid flow rates, T_3 and T_1 deliver already bigger objects with a non-negligible body. Another interesting point to notice is that a significant change due to coalescence around $Q_G/Q_L = 5.0$ is logically observed with T_2 and $T_{2,90°}$ on the two figures of Fig. 15. As far as a_{body} is concerned, a logical inverted behaviour is observed: the injectors that lead to the smallest objects have the smallest body interface at a given ratio. For the highest ratios, long bubbles are formed leading a_{caps} to reach asymptotically zero and becoming logically negligible towards a_{body} that reaches quite logically the maximum value of 11,900 m^{-1} for our channel width independently of the injector like for the evolution of a_{tot}. The two plots of this Fig. 15 illustrate how the different injectors are attracting for tuning the interfacial area to perform local studies of the mass transfer.

5. Conclusions

Different T-junction geometries and their impact on bubble and slug formations in the case of a G–L flow in square micro-channels has been presented. Inlet geometrical characteristics were shown to have a strong impact on the downstream generated unit cell of a segmented flow for a given set of fluid flow rates. Also, for "non-symmetrical" T-junctions, an inversion in the feeding configuration leads to different flow patterns. An attempt to combine all the results in a single scaling law is proposed and a good agreement is obtained for experimental conditions that did not lead to coalescence downstream of the injector.

The total specific surface area seems to be independent of the junction design and feed configuration. Conversely, the distribution of the interfacial surface area among bubble caps and bubble body can be significant at low Q_G/Q_L. Given that different unit cells generated for a given ratio of fluid flow rates could induce many changes in the hydrodynamics (for example recirculation loops intensity and location), it opens new possibilities to perform studies on the local mass transfer for G–L Taylor flow. Numerical and experimental work is in progress in this way.

6. Notations

Latin letters

a	specific surface area ($m^2{}_{interface}/m^3{}_{reactor}$)
A	section (m^2)
a, b	parameters for numerical optimisation (–)
h	height (m)
k	mass transfer coefficient ($m\,s^{-1}$)
L	length (m)
N	number of experiments (–)
P	perimeter (m)
Q	volumetric flow rate ($m^3\,s^{-1}$)
S	section or surface (m^2)
t	time (s)
u	mean fluid velocity (m/s)
V	volume (m^3)
w	width (m)
W	fraction of the channel cross section available for the liquid (gutters+ film) in the region of the bubble body (–)

Greek letters

$\alpha, \alpha', \alpha''$	parameters for numerical optimisation (–)
β, β''	parameters for numerical optimisation (–)
δ	surrounding film thickness far from the corners (m)
ε	phase hold-up (–)
μ	dynamic viscosity (Pa s)
θ	angle between gas and liquid inlets of a T-junction (rad)
σ	superficial tension ($N\,m^{-1}$)

Subscripts

body	body of the gas bubble excluding the two hemispherical caps
bubble	the whole gas bubble
calc	calculated value
caps	hemispherical caps of gas bubble
cont	continuous phase
channel	main channel of the chip
corner	curved corner of the cross section of the bubble body
disp	dispersed phase
exp	experimental value
G	gas
gutter	gutter filled with liquid on the 4 corner of the main channel
nozzle	inlet for gas in a co-axial injector
slug	liquid segment in the Taylor flow
tot	total
TP	two phases
unit cell	volume containing a gas bubble, a liquid slug and 4 gutters

Superscript

ext	external

Dimensionless groups

Bo	Bond number $\left(=\frac{(\rho_L-\rho_G)\cdot g\cdot d^2}{\sigma}\right)$
Ca	capillary number $\left(=\frac{\mu\cdot u}{\sigma}\right)$
Re	Reynolds number $\left(=\frac{\rho\cdot u\cdot d}{\mu}\right)$
We	Weber number $\left(=\frac{\rho\cdot u\cdot d^2}{\sigma}\right)$

Acknowledgements

The authors are grateful to the Region Rhône-Alpes, the CNRS and the École de Chimie Physique Électronique de Lyon (CPE Lyon) for financial support. Acknowledgments are also addressed to Cyril Delattre and Patrick Pouteau from CEA-LETI for a fruitful collaboration in silicon chip fabrication.

Appendix A. Supplementary data

Supplementary data associated with this article can be found, in the online version, at doi:10.1016/j.cej.2010.08.021.

References

[1] M.T. Kreutzer, F. Kapteijn, J.A. Moulijn, J.J. Heiszwolf, Chemical Engineering Science 60 (2005) 5895–5916.

[2] G. Bercic, A. Pintar, Chemical Engineering Science 52 (1997) 3709–3719.

[3] J.M. van Baten, R. Krishna, Chemical Engineering Science 59 (2004) 2535–2545.

[4] G.I. Taylor, Journal of Fluid Mechanics 10 (1961) 161–165.

[5] A. Günther, S.A. Khan, M. Thalmann, F. Trachsel, K.F. Jensen, Lab on a Chip 4 (2004) 278–286.

[6] V. van Steijn, M.T. Kreutzer, C.R. Kleijn, Chemical Engineering Science 62 (2007) 7505–7514.

[7] P. Sobieszuk, P. Cyganski, R. Pohorecki, Chemical Engineering Research and Design 88 (2010) 263–269.

[8] S. Waelchli, P.R. von Rohr, International Journal of Multiphase Flow 32 (2006) 791–806.

[9] L. Sang, Y. Hong, F. Wang, Journal of Microfluidics and Nanofluidics 6 (2009) 621–635.
[10] D. Qian, A. Lawal, Chemical Engineering Science 61 (2006) 7609–7625.
[11] R. Pohorecki, K. Kula, Chemical Engineering Research and Design 86 (2008) 997–1001.
[12] P. Garstecki, M.J. Fuerstman, H.A. Stonec, G.M. Whitesides, Lab on a Chip 6 (2006) 437–446.
[13] T. Kapoor, V.V. Buwa, Proceedings of the Eighth World Congress in Chemical Engineering Montréal, Canada, 2009.
[14] D.M. Fries, P.R. von Rhor, Journal of Microfluidics and Nanofluidics 6 (2009) 27–35.
[15] J. Tan, S.W. Li, K. Wang, G.S. Luo, Chemical Engineering Journal 146 (2009) 428–433.
[16] N. Dietrich, S. Poncin, N. Midoux, H.Z. Li, Langmuir 24 (2008) 13904–13911.
[17] N. Shao, W. Salman, A. Gavriilidis, P. Angeli, International Journal of Heat and Fluid Flow 29 (2008) 1603–1611.
[18] W.B. Kolb, R.L. Cerro, Chemical Engineering Science 46 (1991) 2181–2195.
[19] A.L. Hazel, M. Heil, Journal of Fluid Mechanics 470 (2002) 91–114.
[20] A. Leclerc, Ph.D. Thesis, Université Claude Bernard Lyon 1, Lyon, France, 2007.